



The rock breaking and ROP increase mechanisms for single-tooth torsional impact cutting using DEM

Xiao-Hua Zhu¹ · Yun-Xu Luo¹ · Wei-ji Liu^{1,2}

Received: 24 May 2018 / Published online: 18 May 2019
© The Author(s) 2019

Abstract

Torsional impact drilling is a new technology which has the advantages of high rock-breaking efficiency and a high rate of penetration (ROP). So far, there is no in-depth understanding of the rock-breaking mechanism for the ROP increase from torsional impact tools. Therefore, it has practical engineering significance to study the rock-breaking mechanism of torsional impact. In this paper, discrete element method (DEM) software (PFC2D) is used to compare granite breaking under the steady and torsional impacting conditions. Meanwhile, the energy consumption to break rock, microscopic crushing process and chip characteristics as well as the relationship among these three factors for granite under different impacting frequencies and amplitudes are discussed. It is found that the average cutting force is smaller in the case of torsional impact cutting (TIC) than that in the case of steady loading. The mechanical specific energy (MSE) and the ratio of brittle energy consumption to total energy are negatively correlated; rock-breaking efficiency is related to the mode of action between the cutting tooth and rock. Furthermore, the ROP increase mechanism of torsional impact drilling technology is that the ratio of brittle energy consumption under the TIC condition is larger than that under a steady load; the degree of repeated fragmentation of rock chips under the TIC condition is lower than that under the steady load, and the TIC load promotes the formation of a transverse cracking network near the free surface and inhibits the formation of a deep longitudinal cracking network.

Keywords Torsional impact rock breaking · Mechanical specific energy · Fractal dimension · Microcrack · DEM

1 Introduction

Torsional impact drilling (TID) is a new drilling technology developed on the basis of rotary drilling (Sapinska-Sliwa et al. 2015). In the past 10 years, various torsional impact drilling tools have been developed and achieved good results (Gillis et al. 2004; Schen et al. 2005; Wu et al. 2010). Among them, the invention of the Tork Buster TID tool makes it possible for polycrystalline diamond compact (PDC) bits to drill into deeper and harder formations at a

faster speed. This technology can effectively suppress or even eliminate the stick–slip vibration of bottom drilling tools and improve drilling efficiency and well quality (Ledgerwood et al. 2010; Clayton 2010; Zhu and Liu 2017; Deen et al. 2011). However, researchers have focused more on tool development, field testing and application of this technology. There is no in-depth understanding of the mechanism for the increase in ROP of rock breaking with the torsional impact tools, which makes the application of the technology limited to a certain extent (Zhu and Liu 2017).

In the last 10 years, a large number of scholars have carried out some studies related to rock breakage and torsional impact rock breaking. Zhang et al. (2011) had measured rock stress–strain behavior and rock deformation and strength characteristics under different rock conditions by triaxial stress tests. They showed that the initial fractures influenced the rock crushing effect and the compaction effect also influenced the rock mechanical properties. The influence of the drilling process on the bottom-hole pressure of the rock surface was studied by Akbari et al. (2011). It is pointed out that the rate of penetration (ROP) is a logarithmic function of

Edited by Yan-Hua Sun

✉ Xiao-Hua Zhu
zxhth113@163.com

Yun-Xu Luo
rackluo@foxmail.com

¹ School of Mechatronic Engineering, Southwest Petroleum University, Chengdu 610500, China

² Postdoctoral Research Station for Oil and Gas Engineering, Southwest Petroleum University, Chengdu 610500, China

the bottom-hole pressure. The rock fragmentation processes induced by double drill bits subjected to steady and dynamic loading were investigated using a numerical method by Wang et al. (2011). Wang et al. (2011) compared the effect of rock breaking when there were torsional impact load and no torsional impact load at the same torsion and weight of bit (WOB) by using their ANSYS model. Results showed that the torsional impact can reduce the accumulated energy storage in the drilling pipe, alleviate the stick–slip vibration, and greatly improve the working conditions of the PDC bit. Zhu et al. (2014) established a dynamic simulation model of full-scale PDC bits for dynamic rock breaking using a finite element model (FEM) to research high-frequency torsion impact. The conclusion is that the tensile stress and compressive stress are intersecting when drilling into a hard formation under high-frequency torsional impact, and the tensile stress is the main stress. Bagde and Karekal (2015) studied sandstone crushing under vibration loading through experiments and numerical simulations. It concluded that vibratory loading has benefits in fracturing rock at relatively lower load compared to conventional loading. Fan et al. (2015) used experimental data to establish a multi-fissured particle flow model with different dip angles, and the failure mode in the test process was reproduced by numerical simulation. Yang et al. (2015) presented an experimental investigation of the damage mechanisms of granites under uniaxial tension using a digital image correlation (DIC) method, and the experimental results showed that the damage was related to the strain as well as to the strain gradient. Li et al. (2016) experimentally investigated the fracture process of sandstone specimens containing a pre-cut hole under coupled static and dynamic loads, and the results show that the combined effects of stress concentration around the pre-cut hole and far-field strain generated by static loading promote rock impact damage. Liu et al. (2017) believed that it is feasible to improve the rock-breaking efficiency of an impact crushing device by increasing the impact frequency and rotating torque.

Using a single tooth to cut rock can reflect the local rock-breaking behavior of the drilling bit to a certain extent. There have been some investigations into single-tooth cutting (Lei and Kaitkay 2003; Su and Akcin 2011; Yadav et al. 2018; Zhu and Jia 2013), and some conclusions have been drawn. Therefore, the use of a single tooth instead of an integral drilling bit simplifies the problem to a large extent, but it is still possible to draw relatively accurate conclusions. Meanwhile, using the DEM can well reflect the internal defects and inhomogeneity of the rock.

Therefore, based on the background of above TID technology in this study, DEM software (PFC2D) is used to compare the rock-breaking behavior of granite under steady and torsional impacting conditions. At the same time, the energy consumption to break rock, microscopic crushing

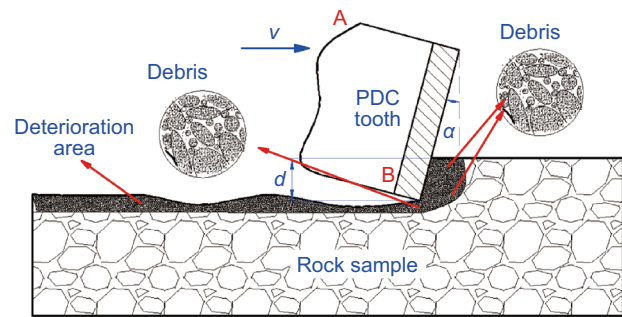


Fig. 1 Single tooth cuts rock

process and chip characteristics as well as the relationship among these three factors for granite under different impact frequencies and amplitudes are discussed. The purpose is to reveal the rock-breaking mechanism of torsional impact in detail and then provide some technical references for the design and work of downhole torsional impact rock-breaking tools.

2 Analysis of the rock-breaking process of TIC

TIC is based on conventional cutting. The difference is that TIC applies a torsional load in accordance with a certain frequency and amplitude of impact to change the loading state between the rock and cutting teeth. Therefore, the TIC model in this paper is based on the following basic assumptions:

1. The impact action time is very short, the rotary motion of the drilling tooth in the rock-breaking process is simplified to a uniform linear motion, and the torsional impact mode is realized by applying an impact velocity with a very short duration of action.
2. The stiffness of the PDC tooth is quite large relative to that of the rock, so the PDC tooth is simplified as a rigid body.
3. The influence of the factors such as drilling fluid, formation pressure, geothermal and other factors affecting the internal energy change of rock are not considered.

2.1 Rock-breaking mode and fracture characteristics of chips

As shown in Fig. 1, a PDC tooth cuts the rock horizontally with a cutting angle α and a cutting speed v . Deterioration occurs in the area below the rock in contact with the tooth, forming a partially degraded area. Due to TIC of the PDC tooth, more or less chips may be generated directly below the PDC tooth, obliquely below the contacting zone of the

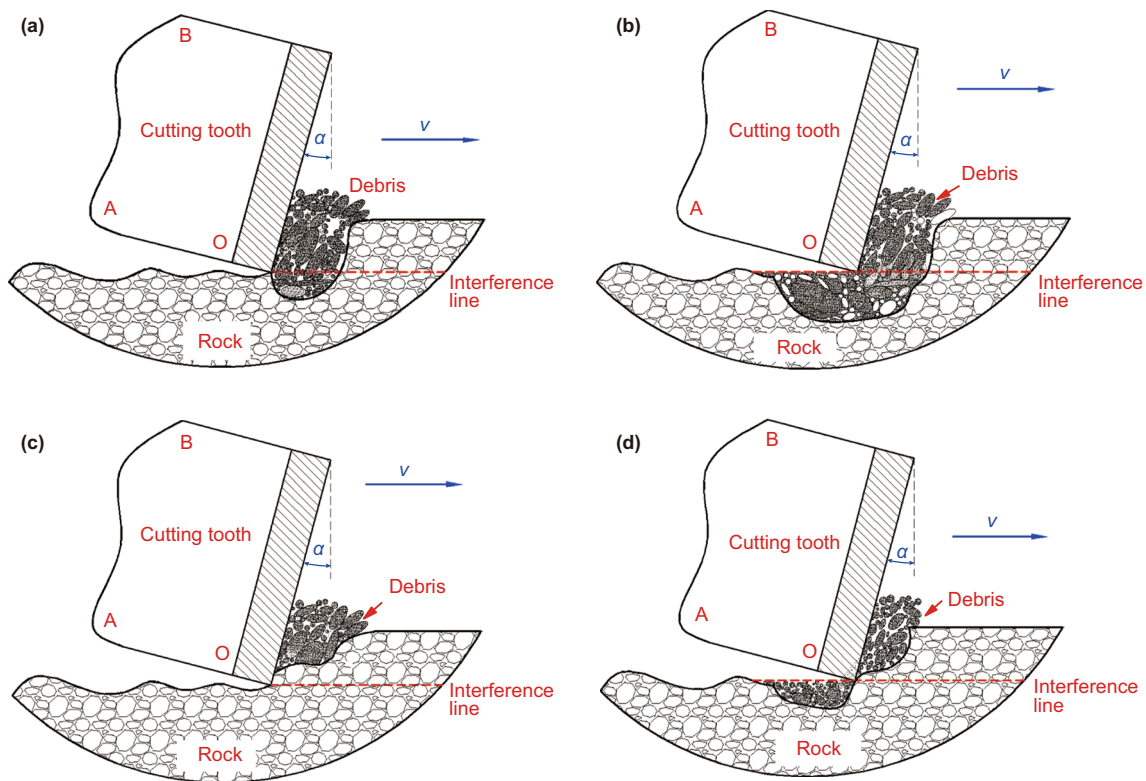


Fig. 2 Four types of modes of action of cutting tooth and rock. **a** Standard type. **b** Interference type. **c** Ideal type. **d** Step type

PDC tooth and the rock, and in the movement direction of the PDC tooth. The generation of these chips will cause the cutters to cause repetitive crushing during the rock-breaking process. The degree of this repeated fragmentation will directly affect the rock-breaking efficiency.

Therefore, according to the characteristics of rotary cutting and the relative position relationship of the cutting tooth and produced chips, the modes of action of the cutting tooth and rock in the rock-breaking process can be divided into four types, as shown in Fig. 2. Meanwhile, the common horizontal line that passes through the bottommost end of the PDC tooth and interfaces with the rock is defined as the interference line, which is the red dotted line in Fig. 2a–d. The first mode of action is given in Fig. 2a, where the produced chips are in the movement direction of the PDC tooth and obliquely below the PDC tooth, as well as the interference line passes through a portion of the chips. This mode of action is defined as the standard type. Figure 2b gives the second mode of action, where the produced chips are in the movement direction of the PDC tooth and obliquely below the PDC tooth and below the entire PDC tooth, as well as the interference line passes through a portion of the chips. This mode of action is defined as the interference type. Figure 2c shows another mode of action where the produced chips are all distributed diagonally above the movement direction of the tooth, but the interference lines do not pass through

the cuttings. This mode of action is called the ideal type. The last mode of action is step type: the produced chips are located diagonally above the movement direction of the tooth and below the entire tooth, and the interference lines do not pass through the debris, as shown in Fig. 2d.

For the above four modes of action, according to the scale of the repeated crushing rate and the total crushing efficiency of the rock after cutting, the crushing efficiency among them is ranked from high to low empirically as: ideal type > interference type > step type > standard type.

For the repeatedly broken rock, the dimensions of rock chips are relatively small after cutting. Therefore, referring to the method of Yan et al. (2008), ranking the produced debris in order from small to large according to the volume of the chips V (mm^3) and the amount of debris whose volume exceeded V is recorded as N . So there is:

$$N \propto x^{-D} \quad (1)$$

where N is the number of chips whose volume exceeds V (mm^3); x is the particle size (mm) corresponding to volume V ; D is the fractal dimension (Sahimi 1992; Xie and Pariseau 1993).

The fractal dimension indicates the degree of fragmentation of the cuttings generated by the cutting tooth. The larger the D is, the higher the degree of fragmentation of the chips is, i.e., the higher the repetitive breaking rate (RBR) of the

rock during the cutting process (Matsui et al. 1982). Meanwhile, due to $x \propto V^{1/3}$, there is:

$$N \propto V^{-D/3} \tag{2}$$

Taking the logarithm of both sides of Eq. (2) gives:

$$\ln(N) = -\frac{D}{3} \ln(V) + B \tag{3}$$

where B is an undetermined constant.

The fractal curve of $\ln N - \ln V$ is made by counting the volume V and number N of the chips; then, the fractal dimension D of the debris can be obtained from the fractal curve. Thus, the relationship between the corresponding rock-breaking efficiency and the size of the debris as well as the RBR can be obtained.

2.2 TIC energy consumption

In order to measure the efficiency of rock breaking in the cutting process, the concept of mechanical specific energy (MSE) is used for reference. The MSE was first proposed by Teale (1965), and it is an important index to measure rock-breaking efficiency. It is defined as the energy consumed by breaking a unit volume of rock, i.e.:

$$MSE = \frac{W}{V} \tag{4}$$

where W is the total work (energy) consumed by the broken rock (mJ); V is the broken volume of rock (mm^3), and the smaller the MSE (mJ/mm^3 or MPa), the higher the rock-breaking efficiency will be.

In addition, a calculation formula based on fractal theory for crushing energy consumption proposed by Yan et al. (2008) is derived:

$$MSE \propto \frac{4 - D}{x_{\max}^{4-D}} \tag{5}$$

where D is the fractal dimension; x_{\max} is the size of the largest piece of rock debris after cutting; MSE is the mechanical specific work.

Substituting $x \propto V^{1/3}$ into Eq. (5) gives:

$$MSE \propto \frac{4 - D}{V_{\max}^{(4-D)/3}} \tag{6}$$

Then, the relationship between the dimension of the rock chips (i.e., the RBR of the cuttings) and the MSE is obtained.

On the other hand, since the study object is granite, it is a hard rock, so the internal cracks can be seen as a result of brittle failure. Meanwhile, all the cutting models used in this paper have the same material parameters. Therefore, it is assumed that the brittle energy consumed by a microcrack in the rock is a certain value. If c microcracks are produced

during the whole cutting process, the brittle energy consumed is as follows:

$$E_B = c\delta \tag{7}$$

where δ is the energy consumed by a microcrack is generated (mJ), supposing it is a constant; c is the number of cracks; E_B is the brittle energy (mJ).

Li et al. (2018) pointed out that the brittle–ductile transformation of rocks has a certain influence on mechanical specific work. Therefore, in order to explore the brittle energy consumption in the total energy used for rock breaking under various cutting conditions in the process of rock breakage, the brittleness energy consumption coefficient (BECC) k is defined as follow:

$$k = \frac{c}{E} = \frac{c}{W} \tag{8}$$

where k is BECC (1/J); E is the energy provided by the drilling tooth (mJ); W is the external work (mJ).

From the brittle energy consumption E_B and the external energy E , it can be concluded that the brittle energy consumption ratio (BECR) in the total energy used for rock breaking is:

$$\eta_B = \frac{E_B}{E} \times 100\% = \frac{c\delta}{W} \times 100\% \tag{9}$$

Meanwhile, the combination of Eqs. (7) and (9) gives:

$$\eta_B = k\delta \times 100\% \tag{10}$$

where η_B is BECR.

PFC2D can neither determine the brittle energy for producing cracks nor accurately calculate the BECR η_B in the total energy of the broken rock. However, we can simply compare the relative energy consumption of brittle energy to total energy when cutting the same rock by the BECC k .

3 Rock parameter calibration and cutting model establishment

The particle flow code (PFC) is a micro-DEM, which is proposed by Cundall and Strack (1980) to simulate the motion and interaction of spherical particles. The Itasca Consulting Group has developed a PFC series of software with the same name based on this method, which is divided into two types: PFC2D and PFC3D.

The calibration of material parameters is an important link in exploring rock breaking by using the discrete element method. This is because the discrete element method is different from the finite element method, and its working principle determines that it cannot directly give the macroscopic property of the rock (Rojek et al. 2011). Meanwhile, since the TID technology can achieve better results in hard

Table 1 UCT results of granite

Height H , mm	Diameter D , mm	Density ρ , kg/m ³	Poisson's ratio ν	Elastic modulus E , MPa	Compressive strength σ_c , MPa
50.05	24.96	2547.6	0.130	15,600.2	104.0

Table 2 BST results of granite

Length L , mm	Diameter D' , mm	Maximum load P_{max} , kN	Tensile strength σ_t , MPa
25.14	24.71	9.141	9.37

Table 3 Calibration results of microparameters of granite

Density ρ , kg/m ³	Friction coefficient μ	Particle modulus E^* , MPa	Particle contact modulus E' , MPa	Radius range R , mm	Radius multiplier λ^*
2547.6	0.577	14,000	14,000	0.1–0.2	1
Stiffness ratio k'	Normal bond strength σ_c^* , MPa	Porosity p_0	Contact stiffness ratio k^*	Cohesive stress c^* , MPa	Friction angle φ , °
2.5	20	0.1	2.5	40	30

formations (Zhu and Liu 2017), granite is selected as the research material. In order to obtain the strength properties of granite, the uniaxial compression tests (UCT) where the compressive strength and elastic properties can be got and the Brazilian splitting tests (BST) where the tensile strength of rock can be tested were performed on granite. The results obtained are shown in Tables 1 and 2.

There are various contact models in PFC2D. This paper uses the flat-joint model, and the particles contacting with others cannot only transmit force, but also transmit torque. The flat-joint model can fit well to rock material with a large tensile compression limit ratio. The advantage of using the flat-joint model to simulate granite is that it can be used to simulate the properties of hard rock and it is easy to monitor the crack growth process. For detailed information on this contact model, please refer to the literature of Potyondy (2012a, b; 2013) and Potyondy and Cundall (2004).

3.1 Material calibration results

Through the virtual simulation experiment, considering the experimental parameters of UCT and BST, the microscopic parameters of the granite simulated by the flat-joint model are finally obtained. The results are shown in Table 3.

The results of the two-dimensional virtual UCT are shown in Fig. 3a, where the colored part characterizes the fragments generated by the rock during loading.

From Fig. 3a, it is known that the fragments generated are mainly distributed on the rock surface and the loading end. Figure 3b, c shows the results of the actual UCT of granite. The results show that the numerical simulation results are in good agreement with the experimental results. Similarly, the results of the two-dimensional vir-

tual BST are shown in Fig. 4a, where the red part characterizes the cracks generated by the rock during loading. In Fig. 4a, the deformed feature of the simulating specimen is that the generated body cracks are approximately at the symmetry center of the specimen, which is consistent with the results of the actual BST in Fig. 4b, c.

In addition, by compiling the fish function, the axial stress (load), number of cracks and axial strain curves of the specimens in the UCT and BST are obtained, as shown in Figs. 5 and 6. As can be seen from Figs. 5 and 6, the number of cracks inside the rock is basically unchanged before reaching the limit load (compressive strength and tensile strength) of the whole rock; however, in a short interval before the specimen reaches the ultimate load, the number of cracks inside the rock increases exponentially until the entire specimen is destroyed. The above results are similar to the tensile damage behavior of red sandstone studied by Peng et al. (2007).

The elastic modulus, the uniaxial compression strength and the splitting strength of the Brazil test of the sample are obtained by two-dimensional virtual UCT and BST. The results are compared with the actual experimental results and are shown in Table 4. From Table 4, we can see that the differences between the elastic modulus, compressive strength and tensile strength of the samples obtained from numerical simulation and actual experiments are 1.49%, 3.36% and 1.28%, respectively, which are all less than 10%. Therefore, the results of the virtual

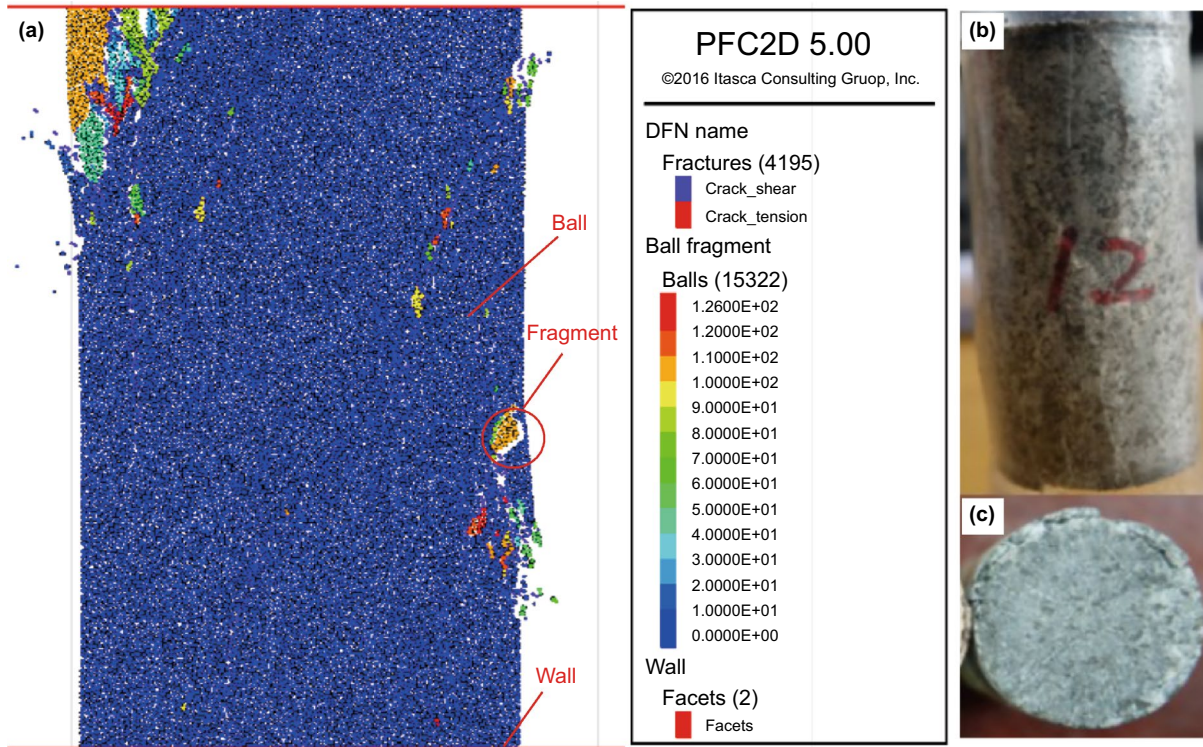


Fig. 3 Numerical results of UCT. a Simulation results. b, c Experiment results

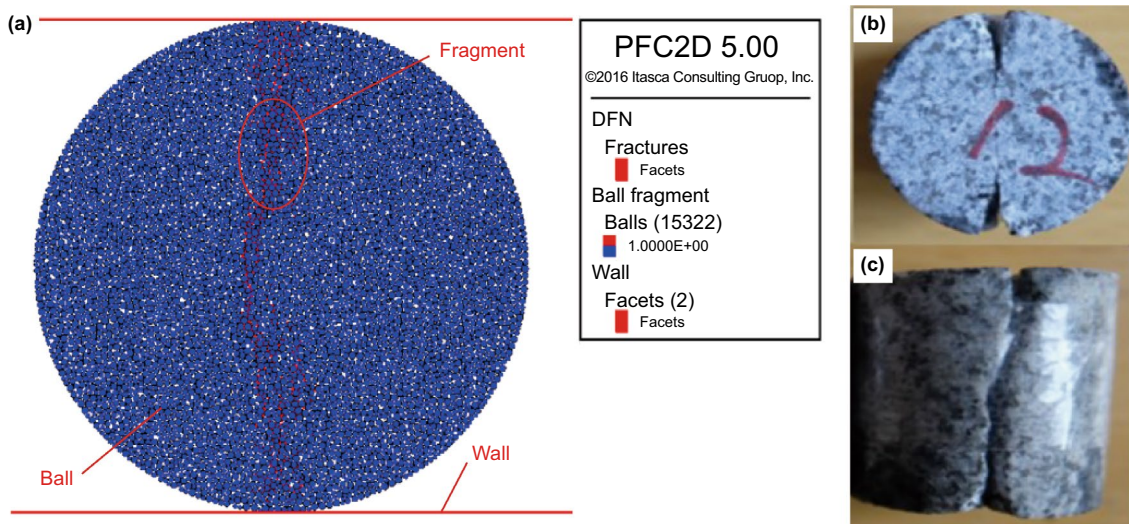


Fig. 4 Numerical results of BST. a Simulation results. b, c Experiment results

experiment show that the deformation characteristics of the two-dimensional virtual experiment are similar to the actual ones and prove that the numerical simulation results have a certain credibility (Zhang 2017). The microscopic parameters of the simulated granite are shown in Table 3.

3.2 Cutting model establishment

In this paper, a cutting model is established to study rock-breaking behavior under TIC. Meanwhile, the broken rock behavior under steady load cutting is compared. The main controlled variables of the model are the impacting

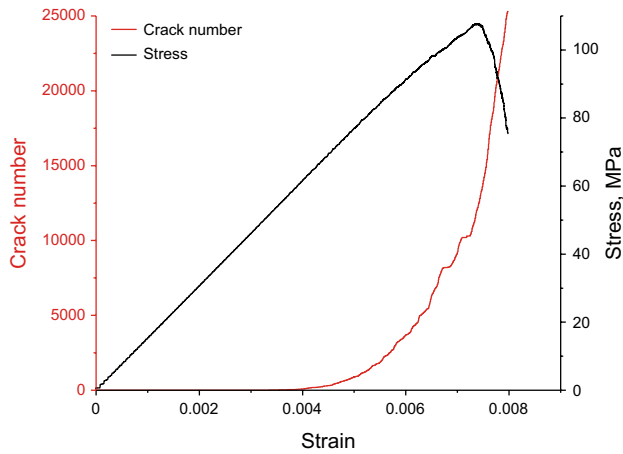


Fig. 5 Calibration curve of UCT

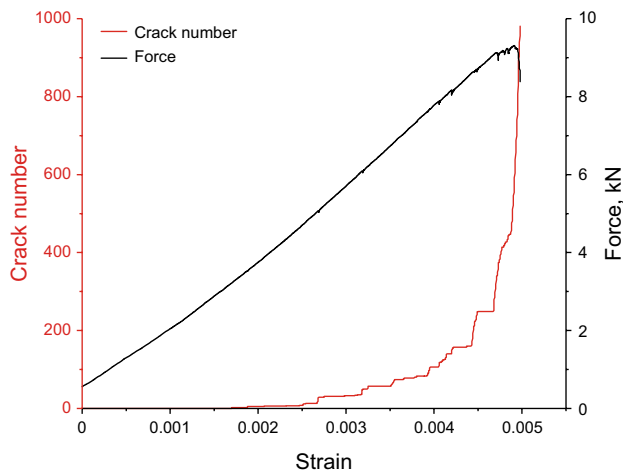


Fig. 6 Calibration curve of BST

Table 4 Comparison of macroscopic parameters between numerical experiments and actual experiments

	Elastic modulus E , MPa	Compressive strength σ_c , MPa	Splitting strength σ_t , MPa
Numerical simulation	15,367.6	107.7	9.49
Actual experiment	15,600.2	104.2	9.37
Relative percentile error, %	1.49	3.36	1.28

frequency and impacting amplitude. Table 5 shows the fixed parameters of the established cutting model. In addition, in the DEM, the calculation principle makes it difficult to apply force directly to the wall (Potyondy and Cundall 2004), so the loading input of this paper is applied by changing velocity.

Table 5 Fixed parameters for TIC model

Rake angle, degree	Cutting depth, mm	Steady load cutting velocity, m/s	Cutting stroke, mm	Single impacting time, ms
15	2	1	20	2

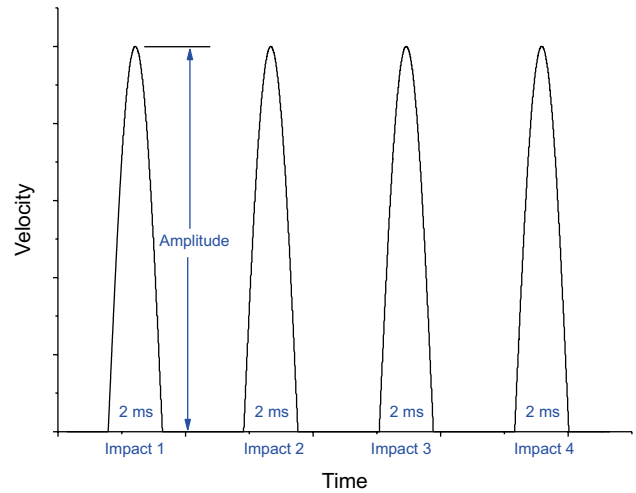


Fig. 7 A load application example when the impacting frequency is four times

Table 6 Load application of TIC model

Impacting amplitude	Loading label at different impacting frequencies			
	1	2	3	4
0.1	T1_1	T2_1	T3_1	T4_1
0.2	T1_2	T2_2	T3_2	T4_2
0.3	T1_3	T2_3	T3_3	T4_3

For steady cutting, its loading type label is Sta. For the TIC model, the impact load is applied by the change of velocity. Figure 7 shows a schematic diagram of a load application with an impacting frequency of four times, where $v_0 = 1$ m/s. The loading type recorded for TIC is denoted by letter ‘T’, and the first number represents the impacting frequency, and the second number represents 10 times the impacting amplitude. For example, T3_2 indicates that during the cutting stroke, the torsional impacting frequency is three times and the impacting amplitude is 0.2, that is, the maximum impact velocity v_{max} is: $v_{max} = (1 + 0.2)v = 1.2$ m/s. TIC loads are shown in Table 6.

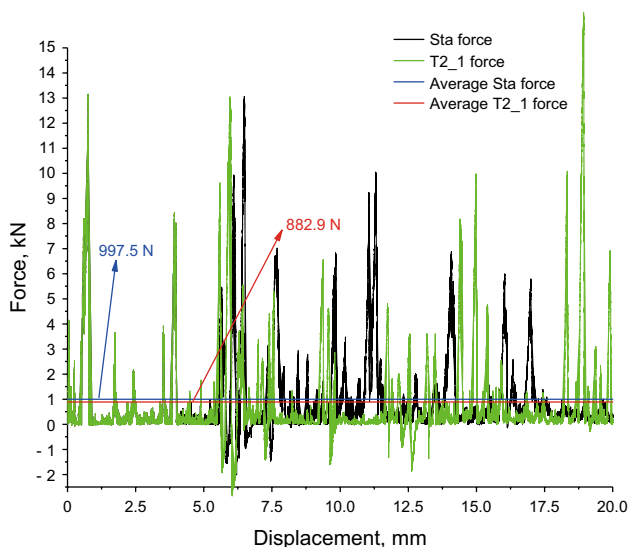


Fig. 8 Tangential force between steady load and T2_1

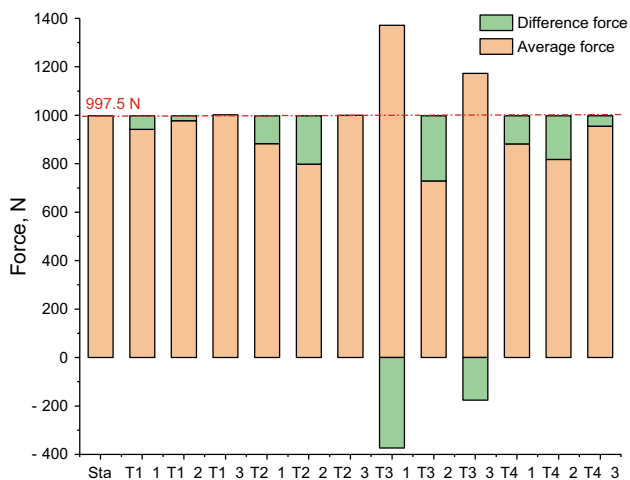


Fig. 9 The mean tangential force of each loading case

4 Results analysis and discussion

4.1 Cutting force and MSE

Figure 8 shows a comparison of the cutting tooth’s force between steady load cutting and T2_1 (i.e., impact frequency two times, impact amplitude 10%). From Fig. 8, the mean values of the cutting forces are 998 and 883 N for the steady loading cutting and T2_1, respectively. When the TIC loading is T2_1, the average cutting force decreases by 11.5% of that when steady cutting. Similarly, Fig. 9 shows the average cutting force of the cutting teeth for each loading condition of TIC and the cutting force difference between steady cutting load and TIC. As shown in Fig. 9, in most cases of the

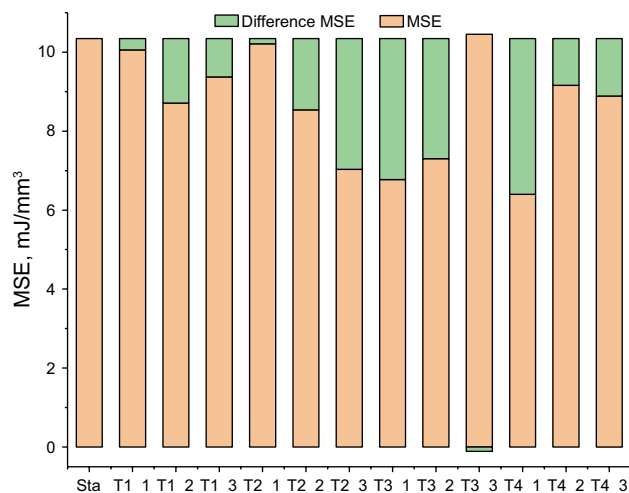


Fig. 10 The MSE of each loading case after cutting

TIC, the cutting force is improved, and the cutting force is a minimum at T3_2. Therefore, the average cutting forces of the cutting tooth under the TIC condition are generally smaller than that under steady load.

Figure 10 shows the MSE of each loading case and the MSE difference between steady load and each TIC case after cutting. From Fig. 10, it can be seen that under different impact frequencies and impact amplitudes, the MSE after cutting is smaller than that under steady load, which is consistent with the conclusion of Yang et al. (2014). The MSE is relatively small at TIC case T2_2 to T3_2. Although the MSE reaches a minimum at T4_1, the effect of the impact amplitude on the MSE shows an unstable trend as the impact frequency increases. This instability is not easy to control or predict. Therefore, in all 13 sets of simulations in this paper, the optimal ranges of loading parameters are T2_2 to T3_2. In the actual project, the impact frequency should not be too large.

From the analysis of Sect. 2.2, it can be seen that the BECC k can be used to characterize the relative amount that the brittle energy consumption takes of the total energy consumption after the rock-breaking process. In order to reveal the influence of different impacting frequencies and impacting amplitudes on the MSE and brittleness energy consumption in the rock-breaking process, the BECC k and MSE are performed in the same coordinate system, as shown in Fig. 11. From Fig. 11, it is known that the BECC k and MSE show an inverse correlation and a symmetrical distribution. That is to say, at the same impacting frequency and impacting amplitude, the smaller the MSE is, the larger the BECC k will be and vice versa. Therefore, the larger the proportion of brittleness to total energy consumption, the smaller the MSE of rock breaking and the higher the efficiency of rock breaking.

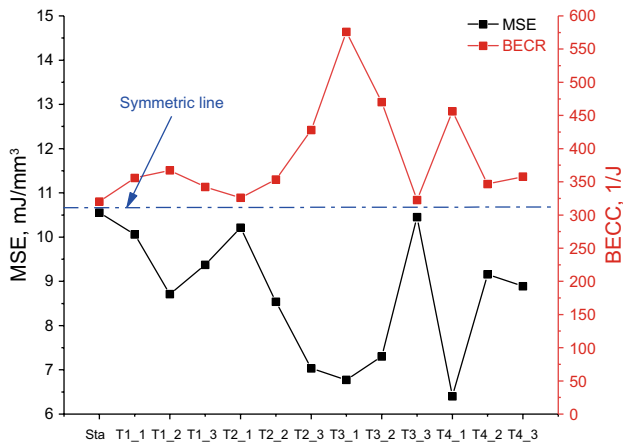


Fig. 11 The MSE and BECC *k* of each loading case

generating chips under several loading cases. The colored parts in the figures are chips (fragments) with different chip dimensions. According to the division of the mode of action between cutting tooth and rock in Sect. 2.1, we can see that the steady load T1_1, T1_3, T2_1 and T2_2 are the standard type, step type, interference type and ideal type of the four modes of action, respectively. The order in which the efficiency of rock breaking from high to low in Sect. 2.1 is equivalent to the order in which MSE from low to high is: ideal type < interference type < step type < standard type. Therefore, the relationship between the mode of action between cutting tooth and rock and the MSE under various loading cases is shown in Fig. 12f. From Fig. 12f, as the loading conditions change, the mode of action between the cutting tooth and rock also changes. In this process, the MSE shows a basin-like change rule that decreases first and

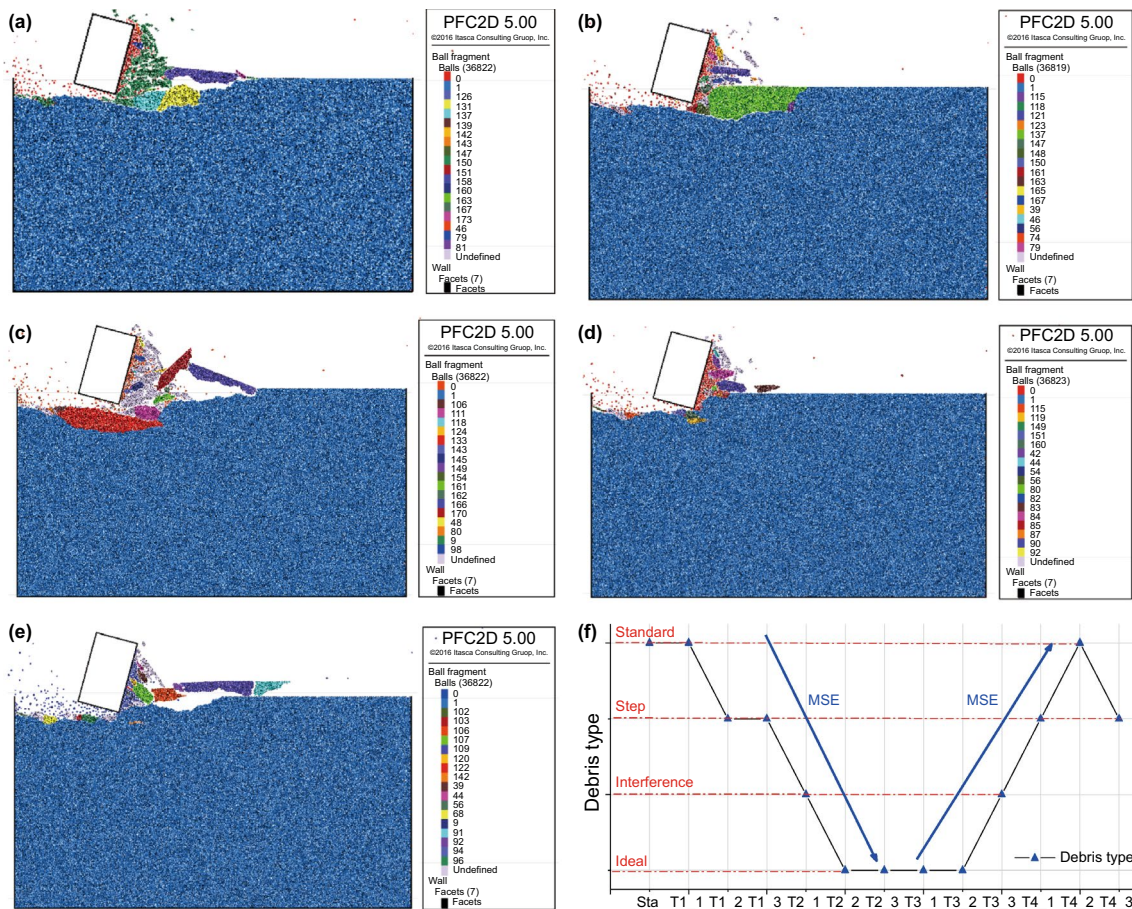


Fig. 12 Acting mode types between tooth and rock under each load case. **a** Sta load case. **b** T1_1 load case. **c** T1_3 load case. **d** T2_1 load case. **e** T2_2 load case. **f** All load case

4.2 The mode of action between cutting tooth and rock and the fractal characteristics of chips

Figure 12a–e shows the results of the cutter cutting rock and

then increases. Under the loading cases of T2_2 to T3_2, the modes of action are all ideal type, the MSE at this time is the smallest, and the rock-breaking efficiency is relatively

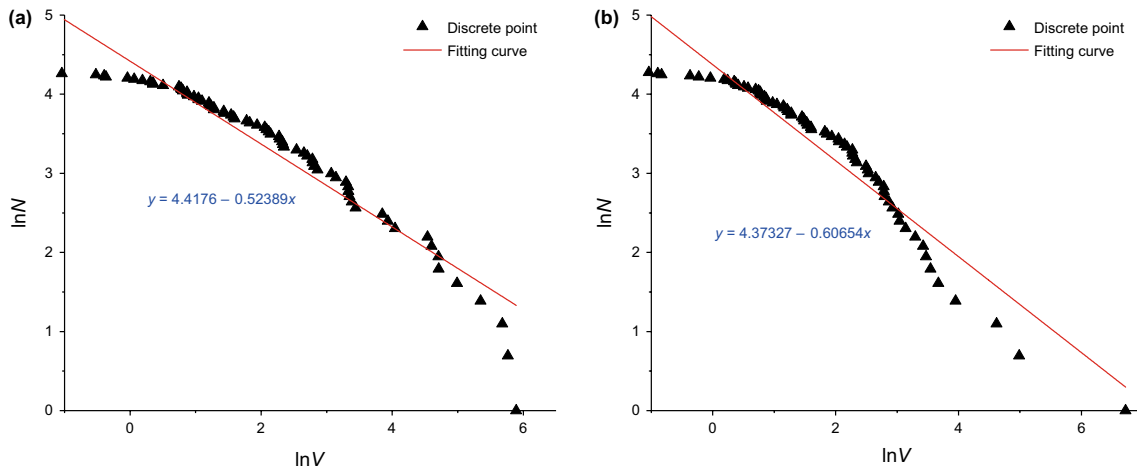


Fig. 13 Fractal curve examples under steady load case and TIC case. **a** Sta load case. **b** T2_2 load case

Table 7 The fractal dimensions of each TIC load case

Loading label	Fractal dimension D	Loading label	Fractal dimension D	Loading label	Fractal dimension D	Loading label	Fractal dimension D
T1_1	1.6959	T2_1	1.7846	T3_1	1.4260	T4_1	1.3923
T1_2	1.5219	T2_2	1.8196	T3_2	1.7848	T4_2	1.5917
T1_3	1.5981	T2_3	1.8003	T3_3	1.8105	T4_3	1.6951

higher. The above conclusions are consistent with the behavior of MSE obtained statistically in Sect. 4.1. This shows that the efficiency of rock crushing is related to the mode of action between cutting tooth and rock.

Meanwhile, the chips produced in the cutting process, according to the method mentioned in Sect. 2.1, can be fitted to the fractal curves of chips after cutting. As shown in Fig. 13, the fractal curves of the chips after cutting under the steady loading case and T2_2 case are plotted, respectively. The fractal dimension of the rock chips under the steady loading case is $3 \times 0.52389 = 1.57167$; and the fractal dimension of chips under the T2_2 case is $3 \times 0.60654 = 1.8196$. Similarly, the fractal dimension under each loading case can be obtained, as listed in Table 7. It can be concluded that the chips are subjected to fractal characteristics after cutting whether it is under steady load or torsional impact load case.

Studying the relationship between MSE after cutting and the fractal dimension of chips is essential to explore the relationship between the rock-breaking efficiency and the size of rock chips. Therefore, Fig. 14a shows the relationship between MSE and the fractal dimension of the chips after cutting under each loading case. It is known that the fractal dimension and MSE change synchronously from Fig. 14a. That is, under the same impacting frequency and impacting

amplitude, the smaller the MSE is, the smaller the fractal dimension will be and vice versa. Therefore, the larger the fractal dimension is, the higher the RBR of the rock is, and the lower the rock-breaking efficiency is.

In addition, in conjunction with Eq. (6) in Sect. 2.1, let $a = \frac{4-D}{V_{\max}^{(4-D)/3}}$. The MSE and value a under each loading case are shown in Fig. 14b. Figure 14a, b have striking similarities. It can be seen from Fig. 14b that the MSE and the value a show a tendency to change synchronously under various loading cases. This proves the correctness of the formula for energy consumption of rock breaking proposed by Yan et al. (2008). This further shows that the RBR of rock in the TIC process is an important factor that affects the crushing efficiency of rock.

4.3 The crack propagation mode

Figure 15 shows the initial crack propagation mode of rock under the steady load case. From Fig. 15a–d, it can be seen the internal crack propagation under steady loading is: Firstly, the cutting tooth comes into contact with the rock, forming a dense crushing zone on the surface of the rock and the cutting teeth; in this area, dense microcracks occur. Then as the cutter advances, transverse cracks are generated from

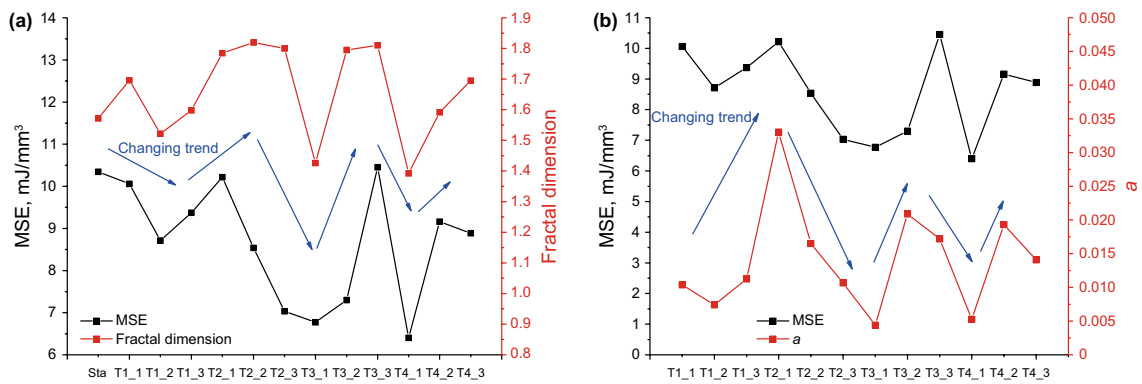


Fig. 14 The relationship between the rock breaking efficiency and size of rock chips. **a** Characterized by the fractal dimension and MSE. **b** Characterized by the value a and MSE

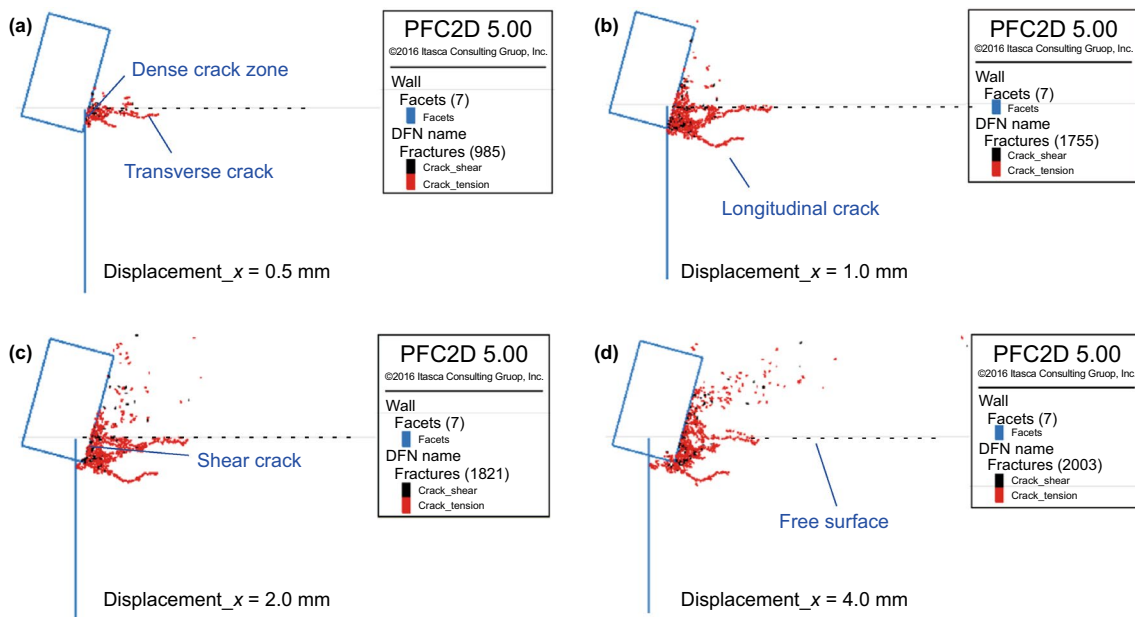


Fig. 15 Initial crack propagation mode of rock under steady load case

the dense crushing zone and extend toward the free surface, as shown in Fig. 15a. After the transverse cracks propagate to the free surface, the dense crack region will continue to generate longitudinal cracks, as shown in Fig. 5b. After that, there is continuous formation of dense cracks, as shown in Fig. 15c, d. It is worth noting that the formation of dense microcracks results in repeated fragmentation of the produced chips and the transformation of the rock from ductility to brittleness.

Figure 16 compares the propagation mode of internal cracks of the rock under the steady load case and the T2_2 load case where the displacement of the cutter is greater than that in Fig. 15. It is noteworthy that Fig. 15 shows the crack propagation behavior inside the rock ranges 0–4 mm under steady load, and the first impacting of T2_2 case occurs at

a cutting stroke of 5 mm. Therefore, the crack propagation behavior during 0–4 mm at T2_2 case is the same as that under steady load, just as Fig. 15.

As the cutting progresses, the cracks of the rock under steady load case develop toward the longitudinal direction of the rock, as shown in Fig. 16a; at the same time, a secondary crack develops on the basis of longitudinal cracks, such as Fig. 16b shows. In the case of TIC, although the longitudinal cracks also expand, the impact causes more cracks to propagate in the transverse direction to form transverse cracks, as shown in Fig. 16c. The laterally spreading cracks continue to expand toward the free surface and eventually form a cracking network near the free surface of the rock, as shown in Fig. 16d. The crack network near the free surface of rock can

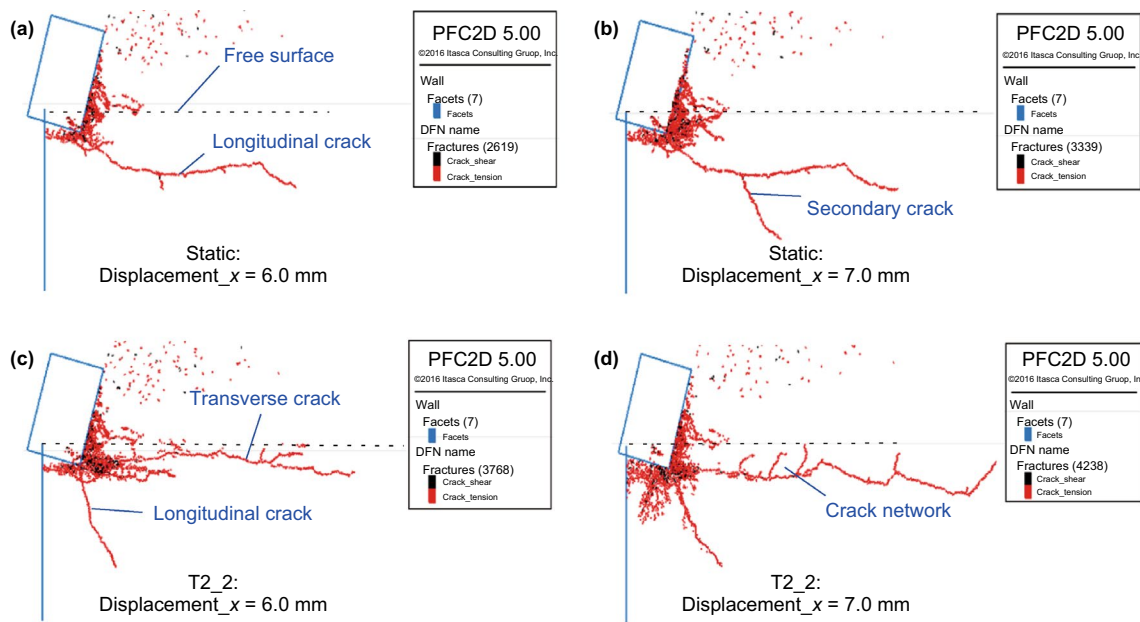


Fig. 16 Comparison of internal crack growth modes in rocks between the steady load and T2_2 load cases

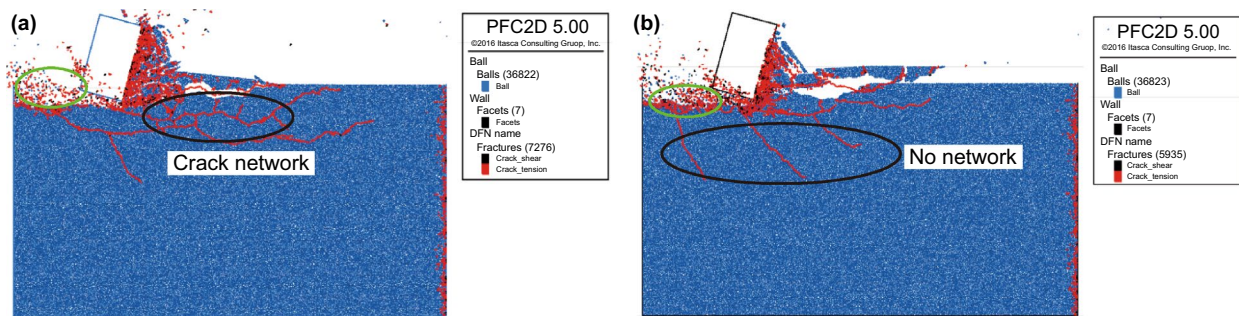


Fig. 17 Internal crack propagation in rock. **a** Steady load case. **b** T2_2 load case

promote the formation of larger size rock chips, making the efficiency of rock-breaking relatively higher.

In addition, Fig. 17 shows the expansion results of cracks in the rock after cutting under the steady load case and T2_2 case, respectively. From Fig. 17a, it can be seen that under the steady loading case, the longitudinal cracks inside the rock and the secondary cracks generating from the longitudinal cracks form a cracking network. However, under the torsional impact loading case, although there are longitudinal cracks in the interior of the rock, the longitudinal cracks do not form intersecting crack networks, as shown in Fig. 17b. Therefore, the torsional impact load promotes the formation of a transverse cracking network near the free surface and inhibits the formation of a deep longitudinal cracking network in the rock.

In terms of the properties of cracks produced under steady load and TIC cases, there are mainly two types: tensile cracks and shear cracks. Shear cracks are mainly

distributed in the dense crack area where the cutter comes into contact with the rock, while tensile cracks are dominant in other places, as shown in Figs. 15, 16 and 17.

The ratio of the number of shear cracks to the total number of cracks under the steady load case was 6.6%. And the ratios of the number of shear cracks to the total number of cracks under each TIC case are listed in Table 8. From Table 8, it is known that cracks in the interior of the rock, both in steady load and in TIC cases, are dominated by tensile cracks, and the number of shear cracks is less than 10%.

5 Conclusion

This paper is based on the background of TID (or TIC) technology. It focuses on the ROP increase mechanism of TID technology. DEM software (PFC2D) is used to

Table 8 The ratio of number of shear cracks to total number of cracks under each TIC load case

Loading label	Ratio of number of shear cracks to total number of cracks, %	Loading label	Ratio of number of shear cracks to total number of cracks, %	Loading label	Ratio of number of shear cracks to total number of cracks, %	Loading label	Ratio of number of shear cracks to total number of cracks, %
T1_1	7.31	T2_1	8.73	T3_1	7.53	T4_1	7.20
T1_2	6.05	T2_2	9.51	T3_2	7.86	T4_2	7.90
T1_3	6.61	T2_3	9.63	T3_3	8.77	T4_3	7.28

compare the breaking of granite under steady and the torsional impacting conditions. Meanwhile, the energy consumption to break rock, microscopic crushing process and chip characteristics as well as the relationship among these three factors for granite under different impacting frequencies and amplitudes are discussed. The main conclusions are drawn as follows:

1. The average cutting force is smaller in the case of torsional impact cutting than that in the case of steady loading. As the impacting frequency increases, there are optimal ranges of impacting frequency and impacting amplitude. In actual projects, the impacting frequency should not be too large.
2. The MSE and the ratio of brittle energy consumption to total energy are negatively correlated: the larger the ratio of energy consumption of brittleness is, the smaller the MSE is, and the higher the rock-breaking efficiency will be.
3. Four types of modes of action between the cutting tooth and rock are introduced. The rock-breaking efficiency is related to the mode of action between the cutting tooth and rock: the mode of action between the cutting tooth and rock at the optimal impacting frequency and amplitude range is the ideal type. Meanwhile, the rock-breaking efficiency is related to the repetitive breaking degree (fractal characteristics) of cutting chips: the greater the fractal dimension is, the higher the repetitive breaking rate of chips is, and the lower the rock fragmentation efficiency will be.
4. The cracks in the interior of the rock, both under steady load and in TIC cases, are dominated by tensile cracks, and the shear cracks are mainly distributed in the zone where the cutter comes into contact with the rock.
5. The reason why the rock-breaking efficiency under the TIC case is higher than that under the steady load case is the ratio of brittle energy consumption under the TIC condition is greater than that under the steady load; the degree of repeated fragmentation of rock chips under the TIC condition is lower than that under the steady load; and the torsional impact load promotes the formation of a transverse cracking network near the free surface and

inhibits the formation of a deep longitudinal cracking network in the rock.

Acknowledgement This study is supported by the National Natural Science Foundation of China (Grant No.51674214), International Cooperation Project of Sichuan Science and Technology Plan (2016HH0008), Youth Science and Technology Innovation Research Team of Sichuan Province (2017TD0014) and Applied Basic Research of Sichuan Province (Free Exploration-2019YJ0520). Such supports are greatly appreciated by the authors.

Open Access This article is distributed under the terms of the Creative Commons Attribution 4.0 International License (<http://creativecommons.org/licenses/by/4.0/>), which permits unrestricted use, distribution, and reproduction in any medium, provided you give appropriate credit to the original author(s) and the source, provide a link to the Creative Commons license, and indicate if changes were made.

References

- Akbari B, Butt SD, Munaswamy K, Arvani F. Dynamic single PDC cutter rock drilling modeling and simulations focusing on rate of penetration using distinct element method. In: U.S. symposium on rock mechanics 45th, San Francisco, Calif, 2011.
- Bagde MN, Karekal S. Fatigue properties of intact sandstone in pre and post-failure and its implication to vibratory rock cutting. *ISRM (India) J.* 2015;4(1):22–7. <http://ro.uow.edu.au/eisapers/4575/>.
- Clayton R. Hammer tools and PDC bits provide stick-slip solution. *Hart's E & P.* 2010;83(2):58.
- Cundall PA, Strack ODL. Discussion: a discrete numerical model for granular assemblies. *Géotechnique.* 1980; 30(3):331–36. <https://doi.org/10.1680/geot.1980.30.3.331>
- Deen CA, Wedel RJ, Nayan A, Mathison SK, Hightower G. Application of a torsional impact hammer to improve drilling efficiency. In: SPE annual technical conference and exhibition, 30 October–2 November, Denver, Colorado, USA, 2011. <https://doi.org/10.2118/147193-MS>.
- Fan X, Kulatilake PHSW, Chen X. Mechanical behavior of rock-like jointed blocks with multi-non-persistent joints under uniaxial loading: a particle mechanics approach. *Eng Geol.* 2015;190:17–32. <https://doi.org/10.1016/j.enggeo.2015.02.008>.
- Gillis PJ, Gillis IG, Knull CJ. Rotational impact drill assembly: US, US6742609. 2004.
- Ledgerwood LW, Hoffmann OJ, Jain JR, Hakam CE, Herbig C, Spencer R. Downhole vibration measurement, monitoring, and modeling reveal stick/slip as a primary cause of PDC-bit damage in today. In: SPE annual technical conference and

- exhibition, 19–22 September, Florence, Italy, 2010. <https://doi.org/10.2118/134488-MS>.
- Lei ST, Kaitkay P. Distinct element modeling of rock cutting under hydrostatic pressure. *Key Eng Mater.* 2003;250(1):110–7. <https://doi.org/10.4028/www.scientific.net/KEM.250.110>.
- Li X, Zhang Q, Li J, Zhao J. A numerical study of rock scratch tests using the particle-based numerical manifold method. *Tunn Undergr Space Technol.* 2018;78:106–14. <https://doi.org/10.1016/j.tust.2018.04.029>.
- Li Y, Peng J, Zhang F, Qiu Z. Cracking behavior and mechanism of sandstone containing a pre-cut hole under combined static and dynamic loading. *Eng Geol.* 2016;213:64–73. <https://doi.org/10.1016/j.enggeo.2016.08.006>.
- Liu S, Chang H, Li H, Cheng G. Numerical and experimental investigation of the impact fragmentation of bluestone using multi-type bits. *Int J Rock Mech Min Sci.* 2017;91:18–28. <https://doi.org/10.1016/j.ijrmms.2016.11.006>.
- Matsui T, Waza T, Kani K, Suzuki S. Laboratory simulation of planetesimal collision. *J Geophys Res Solid Earth.* 1982;87(B13):10968–82. <https://doi.org/10.1029/JB087iB13p10968>.
- Peng RD, Xie HP, Ju Y. Analysis of energy dissipation and damage evolution of sandstone during tension process. *Chin J Rock Mech Eng.* 2007;26(12):2526–31 (in Chinese).
- Potyondy DO, Cundall PA. A bonded-particle model for rock. *Int J Rock Mech Min Sci.* 2004;41(8):1329–64. <https://doi.org/10.1016/j.ijrmms.2004.09.011>.
- Potyondy DO. A flat-jointed bonded-particle material for hard rock. In: 46th U.S. rock mechanics/geomechanics symposium, 24–27 June, Chicago, Illinois, 2012a.
- Potyondy DO. PFC2D flat-joint contact model. In: Itasca Consulting Group, Inc., Minneapolis, MN, Technical Memorandum ICG7138-L, July 26, 2012b.
- Potyondy DO. PFC3D flat-joint contact model (version 1). In: Itasca Consulting Group, Inc., Minneapolis, MN, Technical Memorandum ICG7234-L, June 25, 2013.
- Rojek J, Oñate E, Labra C, Kargl H. Discrete element simulation of rock cutting. *Int J Rock Mech Min Sci.* 2011;48(6):996–1010. <https://doi.org/10.1016/j.ijrmms.2011.06.003>.
- Sahimi M. Brittle fracture in disordered media: from reservoir rocks to composite solids. *Phys A.* 1992;186(1–2):160–82. [https://doi.org/10.1016/0378-4371\(92\)90373-X](https://doi.org/10.1016/0378-4371(92)90373-X).
- Sapińska-Śliwa A, Wiśniowski R, Korzec M, Gajdosz A, Śliwa T. Rotary-percussion drilling method—historical review and current possibilities of application. *AGH Drill.* 2015;32(2):313–22. <https://doi.org/10.7494/drill.2015.32.2.313>.
- Schen AE, Snell AD, Stanes BH. Optimization of bit drilling performance using a new small vibration logging tool. In: SPE/IADC drilling conference, Amsterdam, the Netherlands, 2005. <https://doi.org/10.2523/92336-MS>.
- Su O, Akcin NA. Numerical simulation of rock cutting using the discrete element method. *Int J Rock Mech Min Sci.* 2011;48(3):434–42. <https://doi.org/10.1016/j.ijrmms.2010.08.012>.
- Teale R. The concept of specific energy in rock drilling. *Int J Rock Mech Min Sci Geomech Abstr.* 1965;2(1):57–73. [https://doi.org/10.1016/0148-9062\(65\)90022-7](https://doi.org/10.1016/0148-9062(65)90022-7).
- Wang SY, Sloan SW, Liu HY, Tang CA. Numerical simulation of the rock fragmentation process induced by two drill bits subjected to static and dynamic (impact) loading. *Rock Mech Rock Eng.* 2011;44(3):317–32. <https://doi.org/10.1007/s00603-010-0123-4>.
- Wu X, Paez LC, Partin UT, Agnihotri M. Decoupling stick/slip and whirl to achieve breakthrough in drilling performance. In: IADC/SPE drilling conference and exhibition, 2–4 February, New Orleans, Louisiana, USA, 2010. <https://doi.org/10.2118/128767-MS>.
- Xie H, Pariseau WG. Fractal character and mechanism of rock bursts. *Int J Rock Mech Min Sci Geomech Abstr.* 1993;30(4):343–50. [https://doi.org/10.1016/0148-9062\(93\)91718-X](https://doi.org/10.1016/0148-9062(93)91718-X).
- Yadav S, Saldana C, Murthy TG. Experimental investigations on deformation of soft rock during cutting. *Int J Rock Mech Min Sci.* 2018;105:123–32. <https://doi.org/10.1016/j.ijrmms.2018.03.003>.
- Yan T, Li W, Bi X, Li SB. Fractal analysis of energy consumption of rock fragmentation in rotary drilling. *Chin J Rock Mech Eng.* 2008;27(4):3649–54 (in Chinese).
- Yang G, Cai Z, Zhang X, Fu D. An experimental investigation on the damage of granite under uniaxial tension by using a digital image correlation method. *Opt Lasers Eng.* 2015;73:46–52. <https://doi.org/10.1016/j.optlaseng.2015.04.004>.
- Yang LX, Song JW, He SM, Yu XL, Wang T, Zhang L. Evaluation of parameters for torsional impact to break rock. *Oil F Equip.* 2014;9:1001–3482 (in Chinese).
- Zhang MM. Study of rock breaking simulation of a PDC bit based on discrete element method. Master thesis. 2017. Southwest Petroleum University, China (in Chinese).
- Zhang Q, Mao J, Song QS, Li SJ. Experimental study of dynamic mechanical properties of rock under static and dynamic combination load. *Proc Eng.* 2011;15:3179–83. <https://doi.org/10.1016/j.proeng.2011.08.597>.
- Zhu X, Tang L, Tong H. Effects of high-frequency torsional impacts on rock drilling. *Rock Mech Rock Eng.* 2014;47(4):1345–54. <https://doi.org/10.1007/s00603-013-0461-0>.
- Zhu XH, Jia YJ. 3D mechanical modeling of soil orthogonal cutting under a single reamer cutter based on Drucker-Prager criterion. *Rock Soil Mech.* 2013;41(1):255–62. <https://doi.org/10.1016/j.tust.2013.12.008>.
- Zhu XH, Liu WJ. The rock breaking and ROP rising mechanism for single-tooth high-frequency torsional impact cutting. *Acta Petrolei Sinica.* 2017;38(5):578–86. <https://doi.org/10.7623/syxb201705011> (in Chinese).